

Detection of Interstellar HC₄NC and an Investigation of Isocyanopolyyne Chemistry under TMC-1 Conditions

Ci Xue¹, Eric R. Willis¹, Ryan A. Loomis², Kin Long Kelvin Lee³, Andrew M. Burkhardt³, Christopher N. Shingledecker^{4,5,6}, Steven B. Charnley⁷, Martin A. Cordiner^{7,8}, Sergei Kalenskii⁹, Michael C. McCarthy³, Eric Herbst^{1,10}, Anthony J. Remijan², and Brett A. McGuire^{2,3,11}, Separtment of Chemistry, University of Virginia, Charlottesville, VA 22904, USA; cx5up@virginia.edu

² National Radio Astronomy Observatory, Charlottesville, VA 22903, USA; brettme@mit.edu

³ Center for Astrophysics|Harvard & Smithsonian, Cambridge, MA 02138, USA

⁴ Department of Physics and Astronomy, Benedictine College, Atchison, KS 66002, USA

⁵ Center for Astrochemical Studies, Max Planck Intitute for Extraterrestrial Physics, Garching, Germany

⁶ Institute for Theoretical Chemistry, University of Stuttgart, Stuttgart, Germany

Astrochemistry Laboratory and the Goddard Center for Astrobiology, NASA Goddard Space Flight Center, Greenbelt, MD 20771, USA

⁸ Institute for Astrophysics and Computational Sciences, The Catholic University of America, Washington, DC 20064, USA

⁹ Astro Space Center, Lebedev Physical Institute, Russian Academy of Sciences, Moscow, Russia

¹⁰ Department of Astronomy, University of Virginia, Charlottesville, VA 22904, USA

¹¹ Department of Chemistry, Massachusetts Institute of Technology, Cambridge, MA 02139, USA

Received 2020 March 16; revised 2020 June 25; accepted 2020 June 26; published 2020 September 1

Abstract

We report an astronomical detection of HC_4NC for the first time in the interstellar medium with the Green Bank Telescope toward the TMC-1 molecular cloud with a minimum significance of 10.5σ . The total column density and excitation temperature of HC_4NC are determined to be $3.29^{+8.60}_{-1.20} \times 10^{11}$ cm⁻² and $6.7^{+0.3}_{-0.3}$ K, respectively, using Markov chain Monte Carlo analysis. In addition to HC_4NC , HCCNC is distinctly detected whereas no clear detection of HC_6NC is made. We propose that the dissociative recombination of the protonated cyanopolyyne, HC_5NH^+ , and the protonated isocyanopolyyne, HC_4NCH^+ , are the main formation mechanisms for HC_4NC while its destruction is dominated by reactions with simple ions and atomic carbon. With the proposed chemical networks, the observed abundances of HC_4NC and HCCNC are reproduced satisfactorily.

Unified Astronomy Thesaurus concepts: Astrochemistry (75); Chemical abundances (224); Interstellar medium (847); Dark interstellar clouds (352); Dense interstellar clouds (371); Interstellar molecules (849)

1. Introduction

Understanding the formation and destruction routes of molecules in astronomical environments remains one of the challenging issues in modern astrochemistry. Increasingly sensitive astronomical observations can reveal detailed information about the chemical inventories present in interstellar sources. Laboratory experiments and astrochemical modeling can then work in tandem to uncover the chemical mechanisms underlying these molecular inventories. However, there are still deficiencies in our understanding of the chemistry of interstellar sources. For example, in spite of proposed formation routes through grain chemistry, gas-phase formation routes cannot be ruled out as a viable pathway for the formation of large astronomical molecules (Balucani et al. 2015; Acharyya & Herbst 2017; Coutens et al. 2017, and references therein). The question remains as to how to better model the chemistry present in these astronomical environments and make the models more predictive. In turn, these robust models could then suggest further chemical species to be investigated both in the laboratory and through astronomical observations.

Structural isomers are a promising class of molecules for improving the accuracy of models. Structural isomers contain the same constituent atoms but are arranged in different elemental configurations (Xue et al. 2019). One of the most well studied isomeric pairs in astronomical environments is that of hydrogen cyanide (HCN) and isocyanide (HNC) (Schilke et al. 1992; Turner et al. 1997; Hirota et al. 1998; Herbst et al. 2000; Tennekes et al. 2006; Graninger et al. 2015). At 100 K, under thermal equilibrium conditions, the relative abundance

ratio between HNC and HCN is $\sim 10^{-30}$ (Brown 1977). However, it is well known that under dark cloud conditions, such as those found in the Taurus Molecular Cloud 1 (TMC-1), the abundance ratio approaches ~ 1 (Irvine & Schloerb 1984), indicating that thermodynamic equilibrium certainly does not apply to the two species in these regions (Brown et al. 1989). Instead, measured column densities toward these sources are dominated by the kinetics of chemical reactions in the gas phase; these measurements give observational constraints on the chemical formation and destruction networks (Graninger et al. 2014). As such, measuring the relative abundance ratios for pairs of chemical isomers, and incorporating isomerspecific chemistry into chemical networks, can be a powerful tool to improving the predictive power of these models. Here, we focus on exploiting the cyanide and isocyanide pairs of isomers.

The family of astronomically detected cyanides includes HCN, methyl cyanide (CH₃CN), vinyl cyanide (CH₂CHCN), ethyl cyanide (CH₃CH₂CN), and other species including isocyanogen (CNCN), E-cyanomethanimine (E-HNCHCN), glycolonitrile (HOCH₂CN) and many others (McGuire 2018; Zeng et al. 2019, and references therein). Some of these species are found in high abundance and are readily detectable in a variety of interstellar environments (Miao & Snyder 1997; Araya et al. 2005; López et al. 2014; Hung et al. 2019). In contrast to the numerous detection of cyanides in astronomical environments, there have been very few confirmed detection of isocyanides, such as methyl isocyanide (CH₃NC) (Remijan et al. 2005; Gratier et al. 2013). Most recently, the Protostellar

Interferometric Line Survey observed CH₃NC in a solar-type star, IRAS 16293-2422, for the first time toward a source of this type (Calcutt et al. 2018). Despite that, there have been no successful detections of CH₂CHCH₂NC (Haykal et al. 2013) or CH₃CH₂NC (Remijan et al. 2005; Margulès et al. 2018).

Alongside CH₃CN, one of the most frequently observed families of cyanide species, especially in cold sources, are the cyanopolyynes ($HC_{2n}CN$) (Broten et al. 1978; Little et al. 1978; Bell et al. 1998). Yet, despite their relative ubiquity, the only isocyanide version that has been successfully detected is HCCNC (Kawaguchi et al. 1992), the isomer of HC₃N. Remijan et al. (2005) first searched for isocyanodiacetylene (HC₄NC), the isomer of HC₅N, toward Sagittarius B2(N). To the best of our knowledge, this has been the only attempt to detect this molecule in astronomical environments, setting an upper limit on the abundance ratio to HC₅N as 0.03. In this work, we report the first astronomical detection of HC₄NC using the data available from the GOTHAM (Green Bank Telescope Observations of TMC-1: Hunting for Aromatic Molecules) observational program of TMC-1 (McGuire et al. 2020a). The detection of HC₄NC along with new observations of HCCNC and an upper limit to the abundance of HC₆NC, have been used to better constrain the gas-phase formation models of both cyanopolyynes and isocyanopolyynes ($HC_{2n}NC$) under TMC-1 conditions. The interplay between -CN and -NC formation chemistry can also provide insights into the physical conditions and history of the sources where these species are detected, therefore making new mechanistic insights into -CN versus -NC chemistry particularly relevant for both new and continuing problems such as the HCN/HNC abundance ratio (e.g., Hacar et al. 2020).

In Section 2, we describe the molecular properties of HC₄NC. Section 3 presents the detection of HC₄NC with the GOTHAM observations and the observational analyses. The results of the analyses are used to constrain the new chemical formation network developed to account for the formation of HC₄NC in Section 4. Finally, in Section 5, we summarize our results and describe the next steps in refining the chemical network and searches for larger isocyanopolyynes toward other astronomical sources.

2. Spectroscopic Properties

The HC_4NC molecule has a linear equilibrium structure (Gronowski & Kołos 2006). For this work, transition frequencies of HC_4NC were taken from the CDMS catalog (Müller et al. 2005); the entry was based on Fourier transform microwave (FTMW) spectroscopy data and ab initio calculations reported by Botschwina et al. (1998).

In addition to the molecular structure, Botschwina et al. (1998) also provided estimates of the electric dipole moment. However, the authors did not report the dipole polarizability, which is required for estimating reaction rate coefficients, as will be discussed in Section 4. To this end, we carried out new calculations with the CFOUR (Coupled-Cluster techniques for Computational Chemistry) suite of electronic structure programs (Stanton et al. 2017), employing the coupled-cluster method with single, double, and perturbative triple excitations (CCSD(T)) under the frozen-core approximation, paired with a Dunning's correlation-consistent quadruple- ζ (cc-pVQZ) basis set. At this level of theory, we obtain an equilibrium dipole moment of 3.24 D in agreement with the value of 3.25 D obtained by Botschwina et al. (1998) employing a smaller

Table 1
Calculated Dipole and Polarizability for the Related Cyanopolyynes and Isocyanopolyynes

Parameter	$\mu_e (D)^a$	$\alpha \ (\mathring{A}^3)^b$	Reference
HC ₃ N	3.788	5.848	Woon & Herbst (2009)
HCCNC	2.990	6.221	Woon & Herbst (2009)
HC ₅ N	4.55	9.61	Loison et al. (2014b)
HC ₄ NC	3.24	10.3501	This work
CH_3C_3N	5.041	8.008	Woon & Herbst (2009)

Notes.

^a The equilibrium electric dipole moment in units of debye.

Dunning's triple- ζ (cc-pVTZ) basis set. The small difference between the cc-pVTZ and cc-pVQZ values suggests that the one-electron properties have effectively converged with respect to basis set, thereby lending confidence in our calculations. With the same method and the cc-pVQZ basis set, we obtain a value of $10.3501~\text{Å}^3$ for the average dipole polarizability listed in Table 1.

3. Observations

The capabilities of the Green Bank Telescope (GBT) have expanded the molecular census in TMC-1 and, thereby, increased the known molecular inventory in the interstellar medium (McGuire et al. 2017, 2018). The GBT observations of the GOTHAM project targeted the TMC-1 cyanopolyyne peak (CP) centered at $\alpha_{\rm J2000}=04^{\rm h}41^{\rm m}42^{\rm s}5$, $\delta_{\rm J2000}=25^{\circ}41'26''.8$, where the column densities of the carbon-chain species peak. The GOTHAM spectral line survey covers the GBT X-, K- and Ka-bands with total 13.1 GHz frequency coverage from 7.906 to 29.827 GHz. The beam size varies between $\sim 90''$ at 8 GHz and $\sim 26''$ at 29 GHz. At a uniform 0.05 km s⁻¹ velocity resolution, the rms noise ranges from ~ 2 to 20 mK across the data set. Detailed information concerning the GOTHAM observations and the data calibration can be found in McGuire et al. (2020a).

As presented in Figure 1, we identified three emission features above the noise level of the observations assigned to HC_4NC with the GOTHAM survey. Each feature comprises three hyperfine components of the rotational transition. Table 2 summarizes the spectroscopic properties of the nine transitions. The HC_4NC lines show a good match between the observed frequencies and the calculated frequencies from the CDMS database assuming a systematic local standard of rest velocity $(V_{\rm lsr})$ of 5.8 km s⁻¹.

3.1. Determinations of Column Density and Excitation Conditions

A total of 13 transitions of HC₄NC (see Appendix A) were used to rigorously determine the molecular abundance and excitation conditions using the Markov chain Monte Carlo (MCMC) fitting method described in Loomis et al. (2020). Each of the identified emission features consists of four individual velocity components (Loomis et al. 2020), indicating that TMC-1 is not quiescent and isotropic in terms of physical structure. This is supported by recent CCS and HC₃N observations performed with the 45 m telescope at the Nobeyama Radio Observatory (Dobashi et al. 2018).

 $^{^{}b}$ The average dipole polarizability, in units of \mathring{A}^{3} .

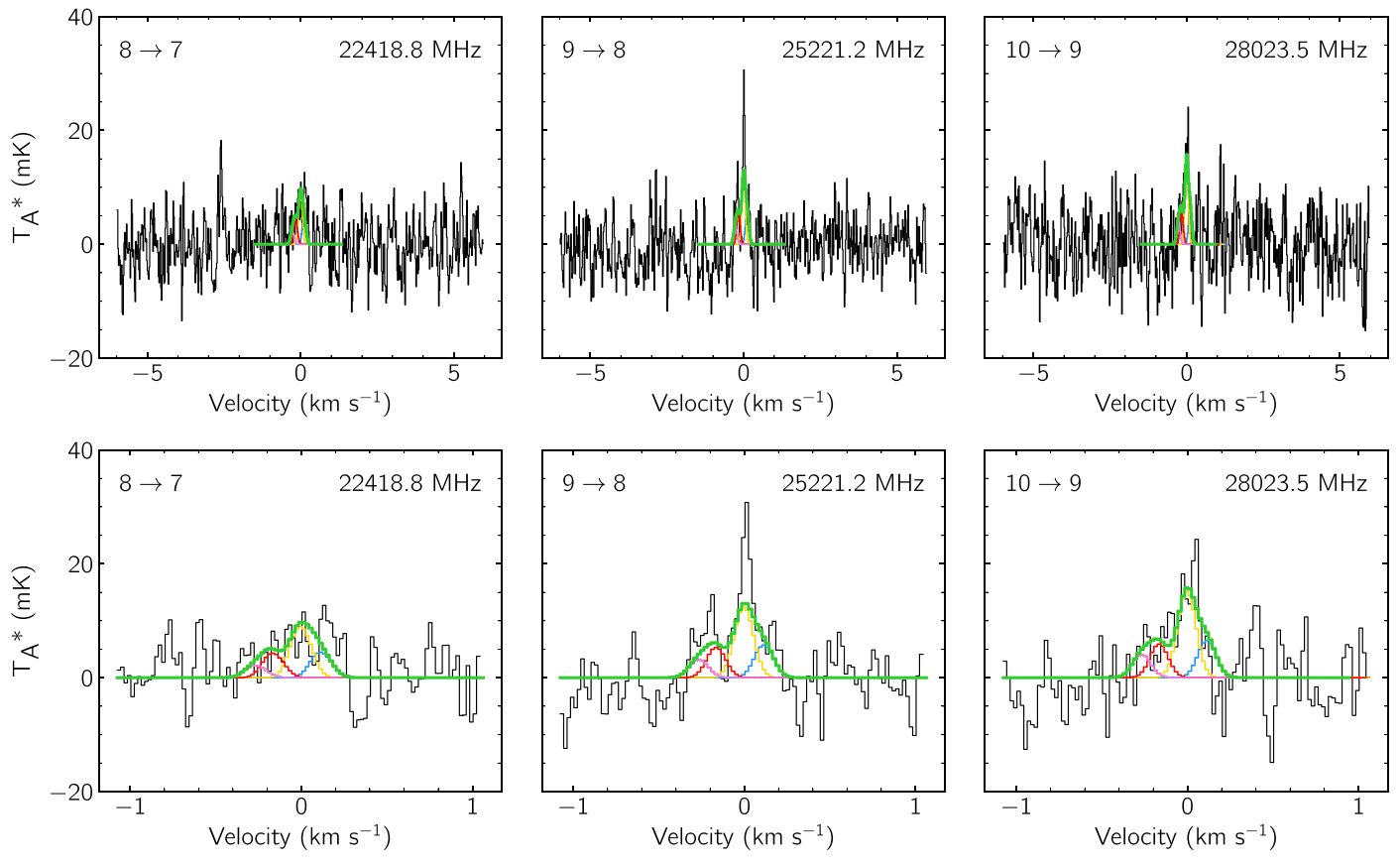


Figure 1. Individual line detections of HC_4NC in the GOTHAM data. The top row shows a wider view to provide context on the noise levels, ~ 5 mK. The bottom row shows the same transitions, zoomed in to show detail. The spectra (black) are displayed in velocity space relative to 5.8 km s⁻¹, and using the rest frequency given in the top right of each panel. Quantum numbers are given in the top left of each panel, neglecting hyperfine splitting. The best-fit model to the data, including all velocity components, is overlaid in green. Simulated spectra of the individual velocity components are shown in: blue (5.63 km s⁻¹), yellow (5.75 km s⁻¹), red (5.91 km s⁻¹), and violet (6.01 km s⁻¹). See Table 3.

Transitions		Frequency	$E_{\rm up}$	$\log_{10} \frac{A_{ul}}{e^{-1}}$	$S_{ij} \mu^2$	
$J' \rightarrow J''$	$F' \rightarrow F''$	(MHz)	(K)		(D^2)	
8 → 7	9 → 8	22418.8438(10)	4.84	-6.1859	94.43	
	$8 \rightarrow 7$	22418.8461(10)	4.84	-6.1927	83.18	
	$7 \rightarrow 6$	22418.8498(10)	4.84	-6.1936	73.24	
$9 \rightarrow 8$	$10 \rightarrow 9$	25221.1790(16)	6.05	-6.0295	105.07	
	$9 \rightarrow 8$	25221.1808(17)	6.05	-6.0350	93.88	
	$8 \rightarrow 7$	25221.1837(17)	6.05	-6.0356	83.88	
$10 \rightarrow 9$	$11 \rightarrow 10$	28023.5067(25)	7.40	-5.8899	115.69	
	$10 \rightarrow 9$	28023.5082(26)	7.40	-5.8943	104.57	
	$9 \rightarrow 8$	28023.5105(26)	7.40	-5.8948	94.52	

Note. The spectroscopic data of the HC₄NC transitions corresponding to the three detected emission features are taken from the CDMS catalog (Müller et al. 2005) and the SPLATALOGUE spectroscopy database (https://www.splatalogue.online).

A uniform excitation temperature $(T_{\rm ex})$ and line width (ΔV) for each velocity component are assumed, while source velocity $(V_{\rm lsr})$, source size, and column density $(N_{\rm T})$ are variable among different velocity components. Therefore, there are 14 free parameters in total to be adjusted in the MCMC analysis. A forward model with 14 free parameters is used to iteratively generate model spectra which are compared with the observations. Posterior probability distributions for each

 $\begin{tabular}{ll} \textbf{Table 3}\\ HC_4NC \ Best-fit\ Parameters\ from\ the\ MCMC\ Analysis \\ \end{tabular}$

Component	(km s^{-1})	Size	$N_T^{\rm a}$ (10 ¹¹ cm ⁻²)	<i>T</i> _{ex} (K)	ΔV (km s ⁻¹)		
C1	$5.628^{+0.045}_{-0.038}$	42+9	$0.30^{+0.19}_{-0.13}$	$6.7^{+0.3}_{-0.3}$	$0.120^{+0.012}_{-0.010}$		
C2	$5.745^{+0.021}_{-0.015}$	21^{+7}_{-8}	$1.35^{+1.38}_{-0.50}$				
C3	$5.907^{+0.038}_{-0.046}$	62^{+20}_{-20}	$0.23^{+0.12}_{-0.12}$				
C4	$6.009^{+0.044}_{-0.032}$	9^{+11}_{-6}	$1.40^{+8.48}_{-1.07}$				
$N_T (\text{Total})^{\mathbf{b}}$	$3.29^{+8.60}_{-1.20} \times 10^{11} \text{ cm}^{-2}$						

Notes. The quoted uncertainties represent the 16th and 84th percentile (1σ for a Gaussian distribution) uncertainties.

parameter and their covariances are generated via several million of these parameter draws, populating the corner plot in Appendix A. The resulting best-fit parameters of each velocity component of HC₄NC are summarized in Table 3. As shown in Figure 1, if we take the noise level measured in each passband into account, the constructed profiles fit reasonably well with

^a Column density values are highly covariant with the derived source sizes. The marginalized uncertainties on the column densities are therefore dominated by the largely unconstrained nature of the source sizes, and not by the signal-to-noise of the observations. See Appendix A for a covariance plot, and Loomis et al. (2020) for a detailed explanation of the methods used to constrain these quantities and derive the uncertainties.

^b Uncertainties derived by adding the uncertainties of the individual components in quadrature.

Table 4
Column Densities and XNC/XCN Ratios

Species	N_{T}	$N_{\rm T}$ $N_{\rm T}$ with the Nobeyama Observations ^a	$N_{\rm T}({\rm XNC})/N_{\rm T}({\rm XCN})$		
~	(cm^{-2})	(cm^{-2})	Observation	High HC ₄ NC BF ^b	Low HC ₄ NC BF ^b
HCCCN	$1.75^{+0.05}_{-0.05} \times 10^{14}$ ^c	$2.34^{+0.82}_{-0.30} \times 10^{14}$			
HCCNC	$3.82^{+1.06}_{-0.53} \times 10^{12}$	$8.51^{+8.87}_{-1.90} \times 10^{12}$	$2.2^{+0.7}_{-0.4}\%$	3.0%	3.0%
HC ₄ CN	$6.69^{+0.13}_{-0.13} \times 10^{13}$ ^c	$5.89^{+1.52}_{-1.10} \times 10^{13}$			
HC ₄ NC	$3.29^{+8.60}_{-1.20} \times 10^{11}$		$0.49^{+1.32}_{-0.19}\%$	2.6%	0.34%
HC ₆ CN	$3.65^{+0.13}_{-0.12} \times 10^{13}$ °	$4.57^{+1.74}_{-0.94} \times 10^{13}$			
HC ₆ NC	$<4.04 \times 10^{11}$		<1.1%		

Notes.

the observed spectra for the individual emission features. A total $N_{\rm T}$ of $3.29^{+8.60}_{-1.20} \times 10^{11}~{\rm cm}^{-2}$ with a $T_{\rm ex}$ of $6.7^{+0.3}_{-0.3}~{\rm K}$ is determined for HC₄NC.

The $N_{\rm T}$ per velocity components show variation on the order of a factor of a few but have consistency in the order of magnitude, unlike the case of HC₃N and CCS presented in Dobashi et al. (2018). The variation of $N_{\rm T}$ arises from the degeneracy between the $N_{\rm T}$ of each component and its source size, found by the MCMC analysis. Without any spatial information to constrain the source sizes, we cannot conclude much about their chemical properties.

In addition to the HC₄NC analysis, we have also analyzed HCCNC and HC₆NC in these observations; the results of these analyses are presented in Appendices B and C. HCCNC is definitively detected with six emission features whereas there is no obvious emission detected for HC_6NC . The N_T for HCCNCis measured to be $3.82^{+1.06}_{-0.53}\times 10^{12}~\text{cm}^{-2}$, while a 2σ upper limit of $<4.04\times 10^{11}~\text{cm}^{-2}$ for the HC₆NC column density is determined. HCCNC has been previously detected in TMC-1 with Nobeyama 45 m observations (Gratier et al. 2016), which reported $N_{\rm T}({\rm HCCNC})$ to be $8.51^{+8.87}_{-1.9} \times 10^{12} \, {\rm cm}^{-2}$, consistent with our GOTHAM result. The column densities listed in Table 4 are the sums of the four detected velocity components, where the column densities of HC₃N and HC₅N are from Loomis et al. (2020). The detection of HCCNC and HC_4NC in GOTHAM data gives column density ratios to their corresponding cyanide isomers of 2.2^{+0.7}_{-0.4}% for HCCNC/HC₃N and $0.49^{+1.32}_{-0.19}\%$ HC₄NC/HC₅N toward TMC-1. The observed results are used to constrain the reaction rate coefficients and branching ratios of the formation routes of HC₄NC, as will be discussed in Section 4.2.

3.2. Visualization of the Detection

To better visualize the detection, and determine a minimum statistical significance, we constructed an intensity- and noise-weighted stacked composite spectrum using the GOTHAM data (Loomis et al. 2020). The spectral stacking was performed in velocity space using the 13 HC₄NC transitions covered by the survey. Another composite line profile using the best-fit parameters was constructed, and used as a matched filter to perform the cross-correlation and determine the statistical significance of the detection (Loomis et al. 2020). The results

are shown in Figure 2, and indicate a minimum significance to the detection of HC_4NC of 10.5σ .

4. Discussion

4.1. Chemical Networks

A number of prior investigations have attempted to address the chemical origins of many of the cyanopolyynes observed in TMC-1 (Takano et al. 1998; Taniguchi et al. 2016; Burkhardt et al. 2018). For example, due to the significant abundance enhancement of HCC 13 CN relative to HC 13 CCN and H 13 CCCN, the formation of HC $_3$ N was suggested to be dominated by the neutral–neutral reaction of C $_2$ H $_2$ and the CN radical (Takano et al. 1998). On the other hand, HC $_5$ N and HC $_7$ N show no such enhancement for the analogous 13 C position, implying that the primary formation route for HC $_5$ N is the dissociative recombination (DR) reaction between the N-bearing hydrocarbon ions and electrons in cold environments (Burkhardt et al. 2018). Furthermore, Loison et al. (2014a) pointed out that the H $_2$ CCN + C \rightarrow HC $_3$ N + H reaction is also involved in producing HC $_3$ N.

On the other hand, the chemistry of the corresponding isocyanopolyynes (HC_{2n}NC) is less well known. Compared with neutral-neutral reactions, reaction schemes involving the DR process of protonated molecular ions such as HC₃NH⁺ and HC₂NCH⁺ are more likely to be the main production mechanisms for HCCNC (Kawaguchi et al. 1992; Gensheimer 1997; Osamura et al. 1999; Vastel et al. 2018). These protonated ions can be formed through ion-molecule reactions such as $HCCH^{+} + HNC/HNC$ and $CH_{3}CN + C^{+}$ (Takagi et al. 1999; Quénard et al. 2017). Even though the chemistry of HC₄NC is less well studied compared to HCCNC, both of them belong to the same homologous series. We therefore assumed analogous formation schemes of HCCNC and HC4NC. In other words, HC₄NC would mainly form through the DR of the protonated cyanopolyynes HC₅NH⁺ and protonated isocyanopolyynes HC_4NCH^+ .

One of the most prevalent destruction mechanisms of cyanoand isocyanopolyynes is ion-molecule chemistry, particularly reactions with C^+ , H_3^+ , and HCO^+ (Woon & Herbst 2009). In addition, as described in Loison et al. (2014b), reactions with carbon atoms are also efficient. Therefore, we extrapolate the mechanisms involving carbon atoms to isocyanopolyynes and

^a The column density estimated by the Bayesian approach of the spectral survey performed with the Nobeyama 45 m dish (Gratier et al. 2016).

^b "High HC_4NC BF" corresponds to the model with a high branching fraction to form HC_4NC in the HC_5NH^+ dissociative recombination, i.e., shown as solid lines in Figure 3, while "Low HC_4NC BF" is the modeled result with a low branching fraction shown as dashed lines in Figure 3.

^c Loomis et al. (2020) estimated the column densities of cyanopolyynes with similar MCMC analyses of the GOTHAM data, assuming the four velocity components are co-spatial.

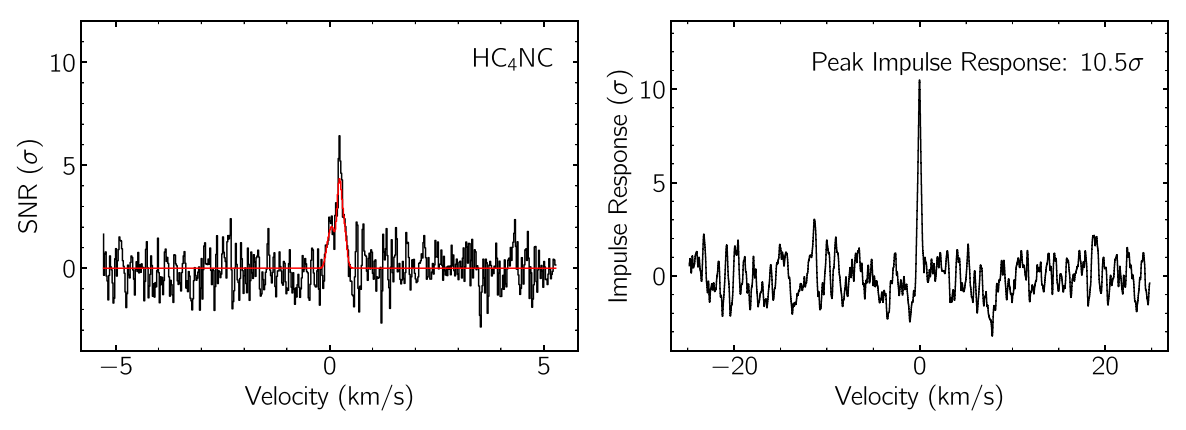


Figure 2. Left: velocity-stacked spectra of HC_4NC in black, with the corresponding stack of the simulation using the best-fit parameters to the individual lines in red. The data have been uniformly sampled to a resolution of 0.02 km s^{-1} . The intensity scale is the signal-to-noise ratio of the spectrum at any given velocity. Right: impulse response function of the stacked spectrum using the simulated line profile as a matched filter. The intensity scale is the signal-to-noise ratio of the response function when centered at a given velocity. The peak of the impulse response function provides a minimum significance for the detection of 10.5σ . See Loomis et al. (2020) for details.

propose that the main destruction mechanisms of HC₄NC are with the ions mentioned above, neutral carbon, and photons.

In this work, we adopted the chemical network of kida.uva.2014 (Wakelam et al. 2015), modified as described in McGuire et al. (2018), as the basis and added or updated the reactions related to HC_3N , HCCNC, HC_5N , and HC_4NC . Note that we introduce HC_4NC as the only isomer of HC_5N in the network. We neglected the other HC_5N isomers to avoid adding more new species of which we have even less knowledge. In the following sections, we will discuss the choices and estimations of the reaction rate coefficients of the formation and destruction pathways of the four molecules of interest. The production and destruction routes regarding HC_4NC are summarized in Table 5 with the corresponding rate coefficients.

4.1.1. Formation Mechanisms: The Dissociative Recombination Reactions

The estimation of the branching ratios and rate coefficients of the HC₃NH⁺ DR are constrained by the laboratory measurements of the DR of DC₃ND⁺ and the consideration of isomerization among the products (Vastel et al. 2019 and references therein). We adopt their values in this paper.

Since HC₃N and HCCNC are both products of the HC₃NH⁺ DR reactions, the HC₅NH⁺ DR, originally included in the kida.uva.2014 network, is amended to include HC₄NC as another product:

The particular choice of the branching ratio is explained below. Based on the potential energy surface of the various HC_3N isomers, Vastel et al. (2019) suggested the branching fraction for the HC_3NH^+ DR forming HC_3N to be 20 times greater than that for the process forming HCCNC (J. Loison 2020, private communication). The energy difference between HC_4NC and HC_5N is calculated to be ~ 114.5 kJ mol $^{-1}$ (or 13,771 K) with the

W1BD thermochemical method, which is similar to the difference between HCCNC and HC₃N, \sim 113.1 kJ mol⁻¹ (or 13,603 K). Because of the lack of a laboratory measurement of the branching ratio in the HC₅NH⁺ DR, we assume a fiducial ratio between the branching fractions for the HC₅N isomers to be 20, analogous to that of the HC₃N isomers. The total rate coefficient for the HC₅NH⁺ DR, $2.0 \times 10^{-6} (T/300)^{-0.7}$ cm³ s⁻¹, and the branching ratios for the other product species are followed as suggested in kida.uva.2014.

The DR of HC₂NCH⁺ is another important pathway leading to HCCNC (Botschwina et al. 1993). In kida.uva. 2014, the rate coefficient for the DR of HC₂NCH⁺ is $6.0 \times 10^{-7} (T/300)^{-0.5}$ cm³ s⁻¹, which seems to be underestimated compared with the experimentally measured rate coefficient for the DR of DC₃ND⁺, $1.5 \times 10^{-6} (T/300)^{-0.7}$ cm³ s⁻¹ (Geppert et al. 2004; Vigren et al. 2012). We expect these rate coefficients to be similar because rate coefficients for DR tend to increase with complexity (Larsson et al. 2012), and because the two cations are of similar complexity. Considering that, we modified the total rate coefficient for the HC₂NCH⁺ DR to be analogous with that of DC₃ND⁺.

Furthermore, we also added HC_4NCH^+ as a secondary precursor of HC_4NC . For the HC_4NCH^+ DR, we assume the total rate coefficient to be consistent with the HC_5NH^+ DR rate coefficient of $2.0 \times 10^{-6} \ (T/300)^{-0.7} \ cm^3 \ s^{-1}$. The channels and branching ratios of the DR of HC_4NCH^+ are assumed to be equal to that of HC_2NCH^+ in the kida.uva.2014 network:

$${\rm HC_4NCH^+} + e^- \rightarrow {\rm C_4H} + {\rm HCN} \quad 38\%$$

 $\rightarrow {\rm C_4H_2} + {\rm CN} \quad 38\%$
 $\rightarrow {\rm HC_5N} + {\rm H} \quad 4\%$
 $\rightarrow {\rm HC_4NC} + {\rm H} \quad 20\%.$

Note that, while HC_4NC can be protonated to form HC_4NCH^+ , the formation of HC_4NCH^+ is dominated by the proposed reaction between CH_3C_3N and the C^+ ion. Thus, consecutive protonation and de-protonation of HC_4NC , resulting in a zero net abundance change, is avoided.

Since the barrierless DR reactions contribute dominantly to the formation of isocyanopolyynes, we emphasize that the determination of the branching ratios are usually more crucial than those of the overall rate coefficients for the case of DR in

Table 5
Summary of the Proposed Dominant Reactions For HC₄NC

Reactions	α	β	γ	Formula Type	k (10 K)
Production Routes:					
$HC_5NH^+ + e^- \rightarrow HC_4NC + H$	4.400×10^{-8}	-0.7	0	3	4.758×10^{-7a}
$HC_4NCH^+ + e^- \rightarrow HC_4NC + H^b$	4.000×10^{-7}	-0.7	0	3	4.326×10^{-6c}
Destruction Routes:					
$HC_4NC + C^+ \rightarrow HC_5N^+ + C$	0.2	2.334×10^{-9}	3.499	4	4.554×10^{-9d}
$HC_4NC + C^+ \rightarrow CNC^+ + C_4H$	0.2	2.334×10^{-9}	3.499	4	4.554×10^{-9d}
$HC_4NC + C^+ \rightarrow C_6N^+ + H$	0.2	2.334×10^{-9}	3.499	4	4.554×10^{-9d}
$HC_4NC + C^+ \rightarrow C_5H^+ + CN$	0.2	2.334×10^{-9}	3.499	4	4.554×10^{-9d}
$HC_4NC + C^+ \rightarrow C_4H^+ + CCN$	0.2	2.334×10^{-9}	3.499	4	4.554×10^{-9d}
$HC_4NC + H_3^+ \rightarrow HC_4NCH^+ + H_2$	1.0	4.420×10^{-9}	3.499	4	4.312×10^{-8d}
$HC_4NC + HCO^+ \rightarrow HC_4NCH^+ + CO$	1.0	1.642×10^{-9}	3.499	4	1.602×10^{-8d}
$HC_4NC + H_3O^+ \rightarrow HC_4NCH^+ + H_2O$	1.0	1.928×10^{-9}	3.499	4	1.881×10^{-8d}
$HC_4NC + H^+ \rightarrow CN + C_4H_2^+$	0.333	7.557×10^{-9}	3.499	4	2.455×10^{-8d}
$HC_4NC + H^+ \rightarrow H_2 + C_5N^+$	0.333	7.557×10^{-9}	3.499	4	2.455×10^{-8d}
$HC_4NC + H^+ \rightarrow C + H_2C_4N^+$	0.333	7.557×10^{-9}	3.499	4	2.455×10^{-8d}
$HC_4NC + He^+ \rightarrow He + C_4H + _{CN}^+$	0.5	3.852×10^{-9}	3.499	4	1.879×10^{-8d}
$HC_4NC + He^+ \rightarrow He + C_4H^+ + CN$	0.5	3.852×10^{-9}	3.499	4	1.879×10^{-8d}
$HC_4NC + C \rightarrow C + HC_5N$	1.000×10^{-10}	0	0	3	1.000×10^{-10e}
$HC_4NC + CRPh \rightarrow CN + C_4H$	3.450×10^{3}	0	0	1	4.485×10^{-14f}
$HC_4NC + Photon \rightarrow CN + C_4H$	9.540×10^{-10}	0	1.830	2	1.076×10^{-17f}

Notes. Definitions of α , β , and γ can be found on the KIDA online database (http://kida.astrophy.u-bordeaux.fr/help.html). Formulae of type 1 and 2 are $k = \alpha \zeta$ and $k = \alpha e^{-\gamma A_{\nu}}$, where k is in s⁻¹, and formulae of type 3 and 4 are $k(T) = \alpha (T/300)^{\beta} e^{-\gamma/T}$ and $k(T) = \alpha \beta (0.62 + 0.4767 \gamma (300/T)^{0.5})$, where k is in cm³ s⁻¹ and T is in K

astronomical environments (Larsson et al. 2012). Nonetheless, although the branching ratios of the related DR reactions are mostly estimated and relatively arbitrary due to the lack of experimental measurement other than for DC_3ND^+ (Geppert et al. 2004), we believe that the values we estimated are reasonable, as supported by the reproduction of observed values discussed below.

4.1.2. Destruction Mechanisms

As previously mentioned, the destruction of the cyano- and isocyanopolyynes is dominated by ion-molecule reactions and reactions with atomic carbon. The reaction coefficient of the related ion-molecule reactions are estimated from Equation (3) from Woon & Herbst (2009), which can be rewritten as

$$k_{\rm D} = 0.4767 \frac{2\pi e \mu_{\rm D}}{\sqrt{2kT\mu}} + 0.62 \times 2\pi e \sqrt{\frac{\alpha}{\mu}},$$
 (1)

where μ_D and α are the dipole moment and the average dipole polarizability of the neutral molecule, respectively, and μ is the reduced mass of the reactants. In addition to adding the new destruction routes proposed for HC₄NC, we also updated the ion–molecule reaction rate coefficients of HCCNC, HC₅N, and CH₃C₃N from the kida.uva.2014 network with this formula and the dipole moments and polarizabilities listed in Table 5. The reaction rate coefficients for the reactions of isocyanopolyynes with carbon atoms are estimated to be the same as those of the

cyanopolyynes (Loison et al. 2014b), while the reaction coefficients for the UV photon dissociation and cosmic-ray ionization reactions of HC_4NC are assumed to be the same as those of HCCNC in kida.uva.2014 respectively.

4.2. Chemical Modeling

We used the three-phase gas-grain astrochemical model NAUTILUS 1.1 (Ruaud et al. 2016) together with our updated network to attempt to reproduce the abundances of HC₄NC and the related species. Physical conditions are assumed to follow typical cold dense cloud conditions, i.e., a gas and dust temperature of 10 K, a gas density $n_{\rm H}$ of $2\times10^4~{\rm cm}^{-3}$, a visual extinction ($A_{\rm v}$) of 10, and a cosmic ray ionization rate (ζ) of $1.3\times10^{-17}~{\rm s}^{-1}$ (Ruaud et al. 2016). We adopted assumed initial elemental abundances in TMC-1 CP as described in Hincelin et al. (2011) with the exception of atomic oxygen. The resulting abundances, with respect to the $N_{\rm T, (H_2)}\sim10^{22}~{\rm cm}^{-2}$ (Gratier et al. 2016), were converted to column densities and compared with the observed values.

We found that both cyano- and isocyanopolyynes are highly sensitive to the initial oxygen elemental abundance. A higher oxygen abundance would result in lower abundances of the HC_3N , HCCNC, HC_5N , and HC_4NC molecules because the majority of C is being locked into CO while reacting with the abundant O. In Figure 3, we present the results of the chemical modeling with an initial C/O ratio of 1.1, in which the model at an age of $\sim 3.5 \times 10^5$ yr gives satisfactory agreement with the

^a The total reaction coefficient of the HC_5NH^+ DR is $2.0 \times 10^{-6} (T/300)^{-0.7}$ cm³ s⁻¹ followed as suggested in kida.uva.2014 while the branching ratio leading to HC_4NC is assumed to be 1/20 of that leading to HC_5N , which is based on the branching fractions for producing HC_3N and HCCNC of the HC_3NH^+ DR (Vastel et al. 2019).

 $[^]b\ HC_4NCH^+$ is mainly produced through the reaction between CH_3C_3N and the C^+ ion.

^c The reaction coefficient of the HC_4NCH^+ DR is assumed to have the same rate coefficient as that of HC_5NH^+ : $2.0 \times 10^{-6} \ (T/300)^{-0.7} \ cm^3 \ s^{-1}$, while the branching ratio is assumed to be similar to that of HC_2NCH^+ , which is included in kida.uva.2014.

^d Rate coefficient estimated from Equation (1) with μ of 3.24 D and α of 10.3501 Å³.

e Rate coefficient same as the family reacting with atomic carbon (Loison et al. 2014b).

f Rate coefficient same as that of the HCCNC + CRPh and HCCNC + photon reactions in kida.uva.2014 respectively.

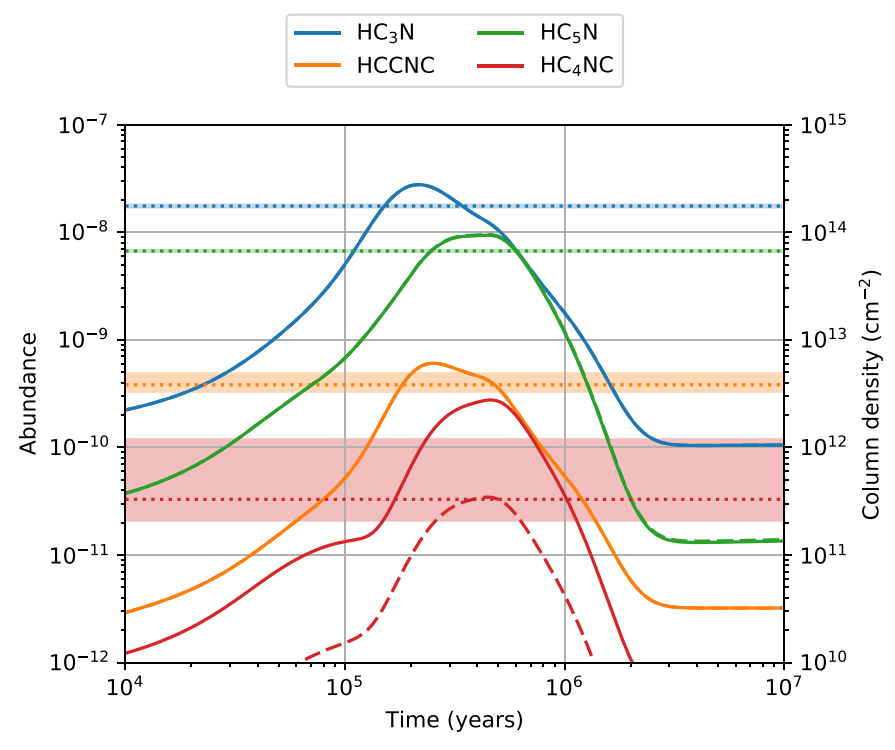


Figure 3. Observed and predicted abundances of HC₃N, HC₅N, HCCNC, and HC₄NC are shown in blue, orange, green, and red respectively. The dotted lines and the shaded regions correspond to the mean and the 1σ range of the observed abundances. The solid and dashed lines represent two models with HC₅N/HC₄NC branching ratios for HC₅NH⁺ DR of 20 and 200 respectively. Note that the predicted abundances of HC₃N, HC₅N, and HCCNC from the two models overlap and are indistinguishable in the figures.

observations for HC₃N, HCCNC, and HC₅N. The initial physical conditions and elemental abundances are all homogeneous among the current series of GOTHAM papers (Burkhardt et al. 2020; Loomis et al. 2020; McCarthy et al. 2020; McGuire et al. 2020b; this work) and have reproduced the observed abundances of the other cyanopolyynes species HC₇N, HC₉N, and HC₁₁N well. Compared with previous astrochemical modeling on TMC-1, the modeled results produce a similar agreement. For example, in Loison et al. (2014b), when assuming the C/O ratio to be 0.95, the peak abundances for HC₃N and HC₅N are \sim 4 × 10⁻⁸ and \sim 7 × 10⁻⁹ respectively and occur at \sim 3 × 10⁵ yr, which are consistent with our results.

The overproduction of HC₄NC could be explained by the defects in the chemical network. Concerning destruction, there could be secondary destruction mechanisms that we have not accounted for, while concerning production, the branching ratios in the related DR processes could be inaccurate. First, the ratio between the branching fraction for forming HC₅N and that for forming HC₄NC in the HC₅NH⁺ DR was assumed to be an analogous value of 20 from the HC₃NH⁺ DR, which could be underestimated. We conducted additional models by varying this ratio and found that increasing it would result in a significant decrease in the simulated abundance of HC₄NC while the increase in HC5N is less significant, as shown in Figure 3. When this ratio is set to be 200, the modeled abundance ratio for HC₄NC/HC₅N can reach 0.34%, which matches well with the observed value, $0.49^{+1.32}_{-0.19}\%$. Therefore, as constrained by the observed abundances, this ratio is suggested to fall within a range of 20-200. Second, neglecting other possible HC₅N isomers in the DR processes would also lead to an overestimation of the branching fractions for forming HC₄NC and HC₅N in the HC₄NCH⁺ DR. A reduction in the

branching ratio could easily reduce the simulated HC_4NC abundance. Experimental studies on the formation and destruction pathways of this molecule are rare, and its detection in TMC-1 therefore highlights the need for more experimental and theoretical work.

4.3. CN/NC Formation Chemistry

In the current study, we have assumed the formation mechanism of HC_4NC to be analogous to that of HCCNC with the understanding that HC_3N and HC_5N , and thus HCCNC and HC_4NC , might have different dominant formation pathways. As such, the model results presented here are only a first attempt at understanding this chemistry with the knowledge that refinements to the models will be necessary as more experimental studies become available.

The current model shows that the HC_nNH^+ DR is the dominant pathway in the formation of HCCNC and HC_4NC , whereas there are several reaction channels contributing to the HCCN and HC_4CN production, and different pathways dominate at different times, in disagreement with what the ^{13}C -isotopologue observation suggests. The resultant model abundance ratios are comparable for HCCNC/HCCCN ($\sim 3.0\%$) and HC_4NC/HC_4CN ($\sim 2.6\%$) at $\sim 3.5 \times 10^5$ yr.

In contrast, the observed HC_4NC/HC_4CN abundance ratio in TMC-1, $0.49^{+1.32}_{-0.19}\%$, is lower than the HCCNC/HCCCN abundance ratio, $2.2^{+0.7}_{-0.4}\%$, within 1σ uncertainty. The uncertainties in the observed ratios are largely introduced by the poor constraint on the spatial distribution of these molecules. One caveat is that, as Remijan et al. (2005) highlighted, a necessary prerequisite to interpret the relative abundance ratio between any molecular species detected in

astronomical environments, including cyanide and isocyanide isomers, is that they must be co-spatial.

A subsequent dedicated search for cyanide and isocyanide pairs in different interstellar sources is justified, because the abundance ratio between cyanide and isocyanide isomers could also vary among sources. For example, the HCCNC/HCCCN abundance ratio toward the L1544 pre-stellar core, ~(3.5–13.8)%, is elevated relative to that in the TMC-1 dark cloud (Vastel et al. 2018). Compared with TMC-1, L1544 is at a later stage along the path of star formation and has a slightly higher excitation temperature of 6–8 K (Vastel et al. 2018). Determining the cause of the variation in CN/NC isomeric ratios may prove useful in constraining the dominant pathways and their dependence on the physico-chemical history of the source.

In addition, studies on other cyanide/isocyanide isomers in TMC-1 would help to address how the NC/CN ratio varies among different pairs of species, such as CH₃CN and CH₃NC. To date, only CH₃CN has been detected toward TMC-1 (Irvine & Schloerb 1984; Gratier et al. 2016), while CH₃NC may be detected as the GOTHAM survey progresses.

5. Summary

In this paper, we report the astronomical detection of HC_4NC for the first time in the interstellar medium using the GOTHAM survey at a minimum significance of 10.5σ . Three emission features above the noise level of the observations are assigned to HC_4NC . Our analysis indicates a total of four distinct velocity components contribute to the emission signal observed for this species. The observed ratio between HC_4NC and its cyanopolyyne counterpart HC_5N is $\sim 0.49^{+1.32}_{-0.19}\%$ while the observed relative abundance ratio between HCCNC and HC_3N is $\sim 2.2^{+0.7}_{-0.4}\%$.

The synthesis of the HC_4NC molecule is linked to the chemistry of the protonated cyanides and isocyanides. We attempted to reproduce the observed abundances of the selected cyano- and isocyanopolyynes with the inclusion of DR as major formation routes and ion-molecule reactions, as well as reactions with atomic carbon as dominant destruction routes. We are aware that HC_3N and HC_5N have different dominant formation pathways whereas the chemical network of HC_4NC in the current study is assumed to be analogous to that of HCCNC. The similar molecular structure of the two isocyanopolyynes makes it the best assumption we can posit.

The chemical modeling presented reproduces the observed abundance of HC₄NC within an order of magnitude. The result of the chemical modeling suggests that the considered formation and destruction routes are reasonable and relevant for HC₄NC and has enabled us to constrain the reaction rate coefficients to some extent. With the increasing number of detected cyano- and isocyanopolyynes in astronomical environments, accurate laboratory measurements of the rate

coefficients and branching ratios for reactions of interest would certainly help to better reproduce the observed results.

A.M.B. acknowledges support from the Smithsonian Institution as a Submillimeter Array (SMA) Fellow. M.C.M and K.L.K.L. acknowledge financial support from NSF grants AST-1908576, AST-1615847, and NASA grant 80NSSC18K0396. Support for B.A.M. was provided by NASA through Hubble Fellowship grant #HST-HF2-51396 awarded by the Space Telescope Science Institute, which is operated by the Association of Universities for Research in Astronomy, Inc., for NASA, under contract NAS5-26555. C.N.S. thanks the Alexander von Humboldt Stiftung/Foundation for their generous support, as well as V. Wakelam for use of the NAUTILUS v1.1 code, C.X. is a Grote Reber Fellow, and support for this work was provided by the NSF through the Grote Reber Fellowship Program administered by Associated Universities, Inc./National Radio Astronomy Observatory and the Virginia Space Grant Consortium. E.H. thanks the National Science Foundation for support through grant AST 1906489. S.B.C. and M.A.C. were supported by the NASA Astrobiology Institute through the Goddard Center for Astrobiology. The National Radio Astronomy Observatory is a facility of the National Science Foundation operated under cooperative agreement by Associated Universities, Inc. The Green Bank Observatory is a facility of the National Science Foundation operated under cooperative agreement by Associated Universities, Inc.

Appendix A MCMC Fitting Detail for HC₄NC

A total of 13 transitions (including hyperfine components) of HC₄NC were covered by GOTHAM observations at the time of analysis and were above the predicted flux threshold of 5%, as discussed in Loomis et al. (2020). Of these transitions, none was coincident with interfering transitions of other species, and thus a total of 13 transitions were considered. Observational data windowed around these transitions, spectroscopic properties of each transition, and the partition function used in the MCMC analysis are provided in the Harvard Dataverse repository (GOTHAM Collaboration 2020). A corner plot of the parameter covariances and their distribution for the HC₄NC MCMC fit is shown in Figure A1. Worth noting are the strong covariances between the column density and the source size for sources #2 and #4. The poor constraint on these source sizes leads to a large uncertainty in the total column density. Future detections of lines at lower or higher frequencies to anchor the source size fit (through measured beam dilution) would greatly enhance the precision of the column density measurement.

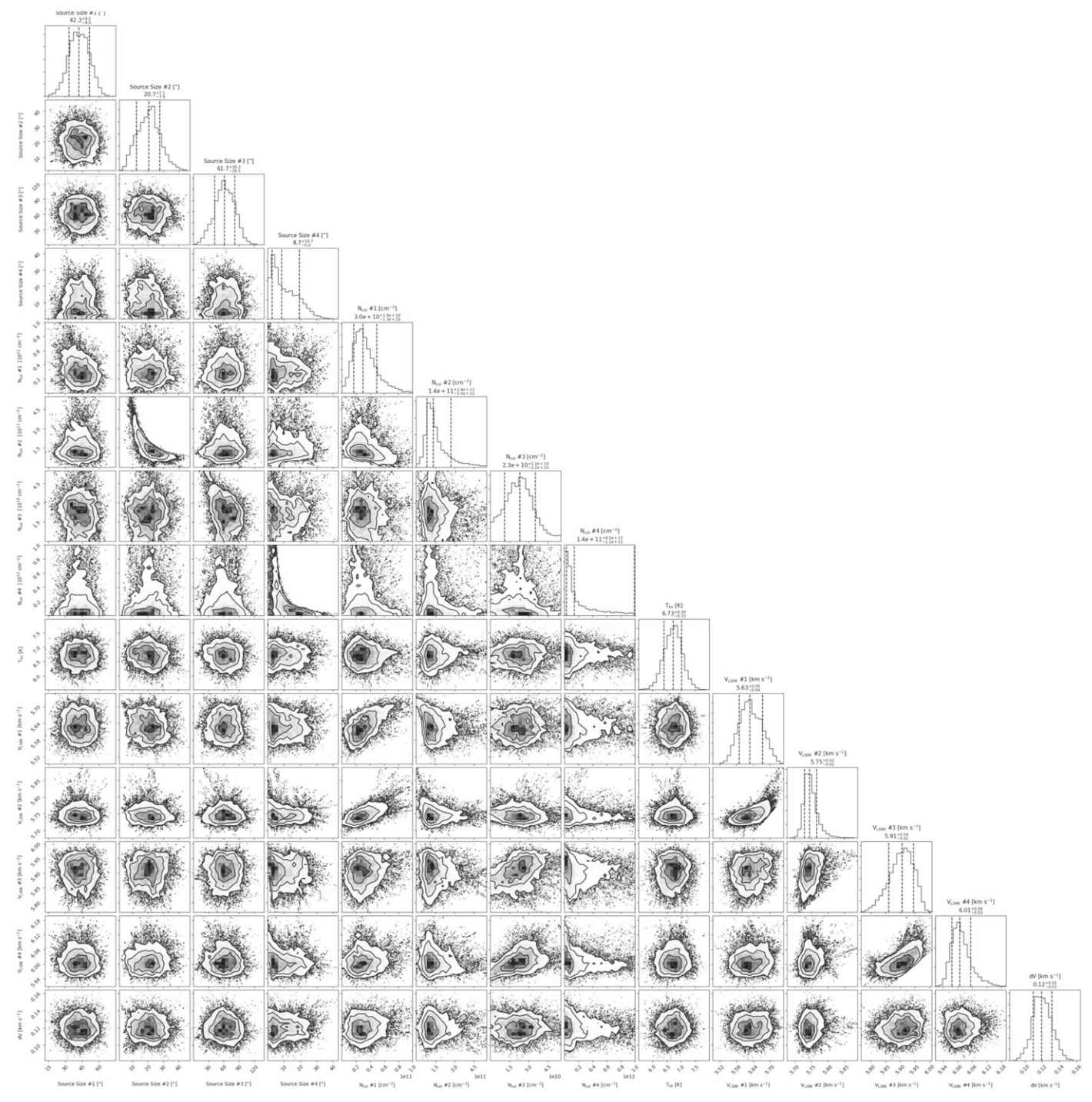


Figure A1. Parameter covariances and marginalized posterior distributions for the HC_4NC MCMC fit; 16th, 50th, and 84th confidence intervals (corresponding to $\pm 1\sigma$ for a Gaussian posterior distribution) are shown as vertical lines.

Appendix B HCCNC Analysis Results

An identical analysis to that for HC₄NC was carried out for HCCNC. Six emission features contributed by the nine rotational transitions (including hyperfine components) of HCCNC are well detected above the noise, as shown in Figure B1. The top three panels are the three hyperfine components of the 1–0 transition respectively while the bottom panel shows all the hyperfine components of the 3–2 transition. The spectroscopic properties of the nine transitions are summarized in Table B1.

Of these transitions, six are above the 5% threshold, which was uniformly applied to the whole GOTHAM data set, and were therefore considered for the MCMC fitting and spectral stacking process, the data used in which are available in GOTHAM Collaboration (2020). The resulting best-fit parameters are given in Table B2. The noise level of the $1_0 \rightarrow 0_1$ spectrum is $\sim\!\!3$ mK, which accounts for the apparent difference seen between the constructed and observed profiles. The stacked spectrum and matched filter results are shown in Figure B2, while a corner plot of the parameter covariances for the HCCNC MCMC fit is shown in Figure B3.

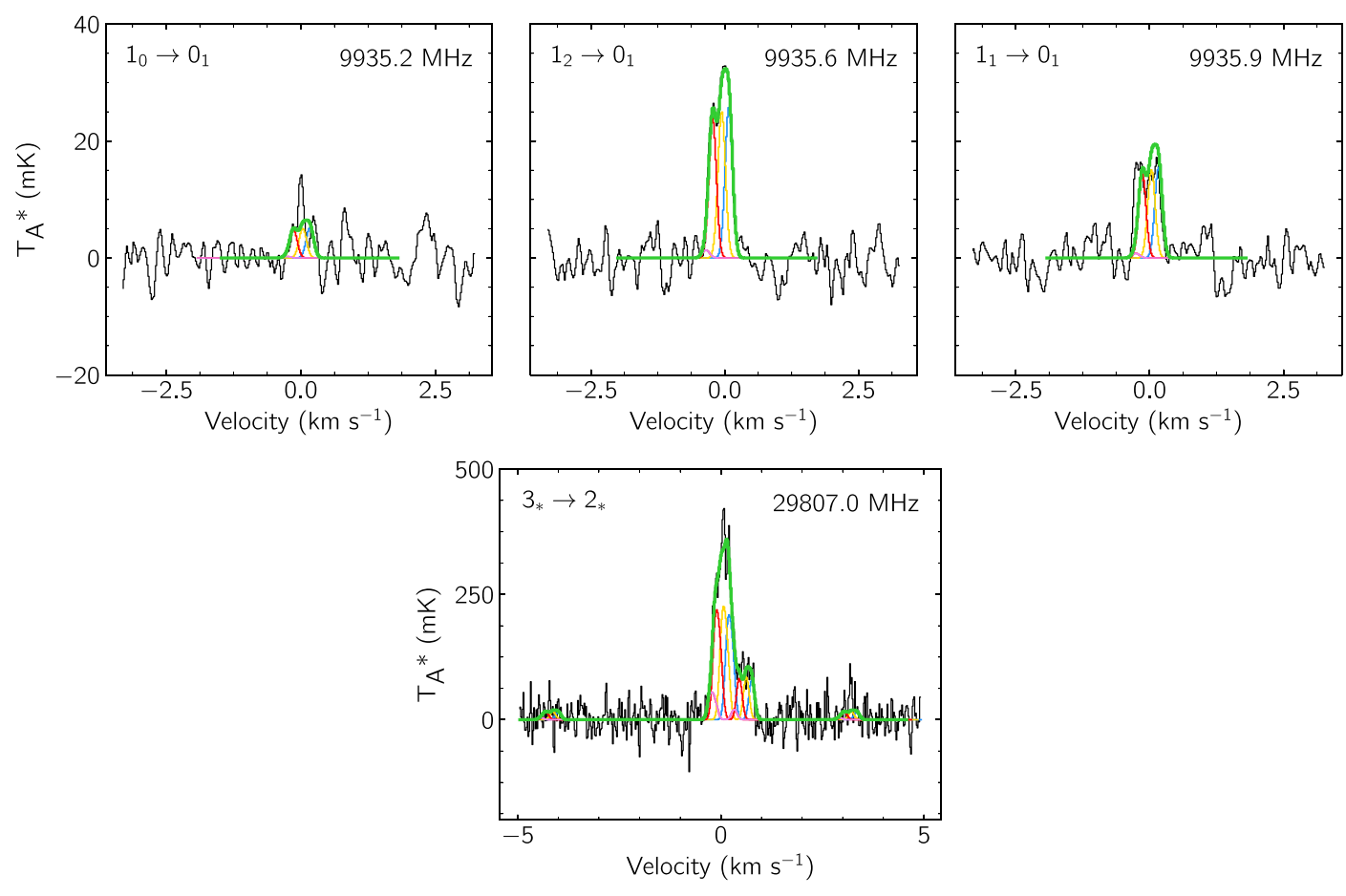


Figure B1. Similar to Figure 1. Individual line detections of HCCNC in the GOTHAM data. The observed spectra (black) are displayed in velocity space relative to 5.8 km s⁻¹ and the simulated spectra of the individual velocity components are shown in blue (5.62 km s⁻¹), yellow (5.76 km s⁻¹), red (5.93 km s⁻¹), and violet (6.05 km s⁻¹), and are summarized in Table B2, with the best-fit model including all velocity components overlaid in green.

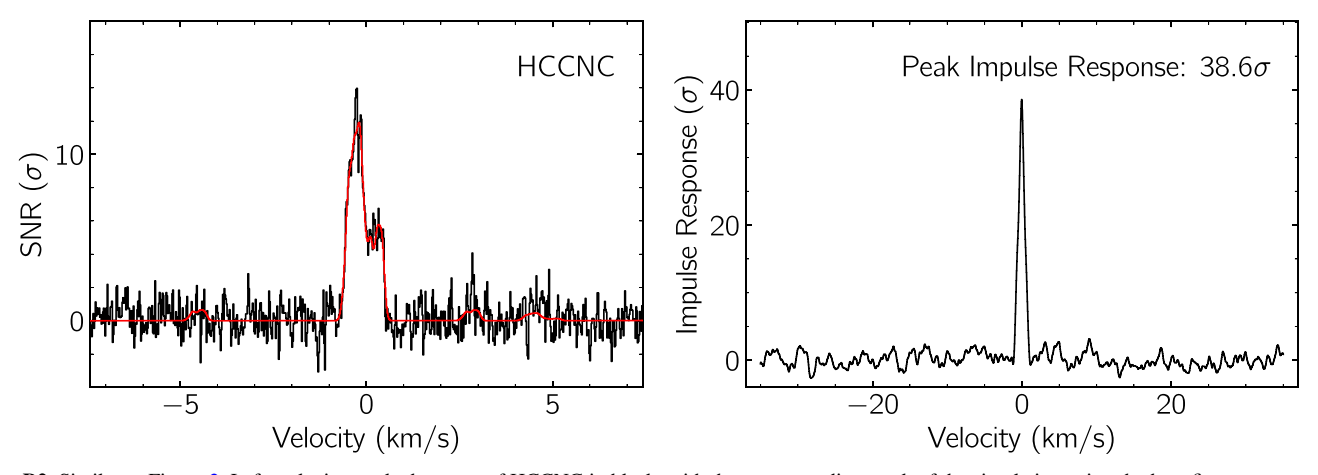


Figure B2. Similar to Figure 2. Left: velocity-stacked spectra of HCCNC in black, with the corresponding stack of the simulation using the best-fit parameters to the individual lines in red. Right: impulse response function of the stacked spectrum using the simulated line profile as a matched filter. The peak of the impulse response function provides a minimum significance for the detection of 38.6σ .

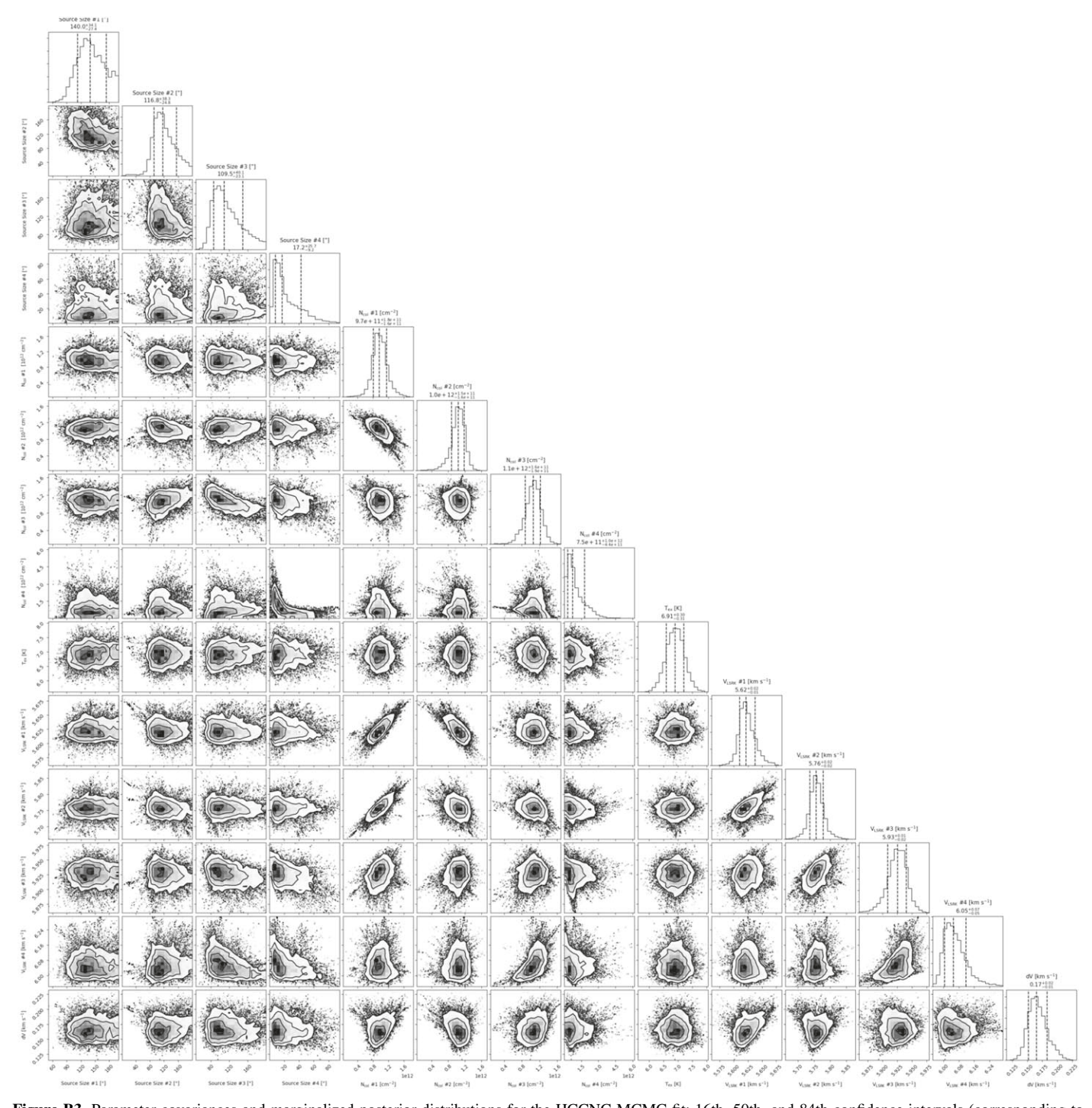


Figure B3. Parameter covariances and marginalized posterior distributions for the HCCNC MCMC fit; 16th, 50th, and 84th confidence intervals (corresponding to $\pm 1\sigma$ for a Gaussian posterior distribution) are shown as vertical lines.

Table B1
Spectroscopic Properties of the HCCNC Lines

Transitions		Frequency	$E_{\rm up}$	$\log_{10} \frac{A_{ul}}{s^{-1}}$	$S_{ij}\mu^2$
$J' \rightarrow J''$	$F' \rightarrow F''$	(MHz)	(K)	-10 s 1	(Debye ²)
$1 \rightarrow 0$	0 → 1	9935.2000(150)	0.48	-7.4859	2.86
$1 \rightarrow 0$	$2 \rightarrow 1$	9935.6270(150)	0.48	-7.4859	14.31
$1 \rightarrow 0$	$1 \rightarrow 1$	9935.9100(150)	0.48	-7.4858	8.59
$3 \rightarrow 2$	$2 \rightarrow 2$	29806.5354(122)	2.86	-6.7535	2.86
	$2 \rightarrow 3$	29806.8398(39)	2.86	-8.2976	0.08
	$4 \rightarrow 3$	29806.9503(20)	2.86	-5.9454	33.11
	$3 \rightarrow 2$	29806.9615(20)	2.86	-5.9965	22.89

Table B1 (Continued)

Transitions		Frequency	E_{up}	$\log_{10} \frac{A_{ul}}{e^{-1}}$	$S_{ii}\mu^2$
$J' \rightarrow J''$	$F' \rightarrow F''$	(MHz)	(K)	s -	(Debye ²)
	2 → 1	29807.0089(25)	2.86	-6.0211	15.45
	$3 \rightarrow 3$	29807.2660(89)	2.86	-6.8996	2.86

Note. The spectroscopic data of the HCCNC transitions corresponding to the six detected lines are taken from the JPL catalog (https://spec.jpl.nasa.gov) and the SPLATALOGUE spectroscopy database, which are based on the FTMW and millimeter-wave measurements of Guarnieri et al. (1992) and Kruger et al. (1993).

 Table B2

 HCCNC Best-fit Parameters from the MCMC Analysis

Component	(km s^{-1})	Size (")	$(10^{12} \mathrm{cm}^{-2})$	T _{ex} (K)	$\frac{\Delta V}{(\text{km s}^{-1})}$
C1 C2 C3 C4	$5.622^{+0.016}_{-0.011}$ $5.756^{+0.022}_{-0.017}$ $5.926^{+0.015}_{-0.017}$ $6.051^{+0.066}_{-0.045}$	$140_{-27}^{+34} \\ 117_{-25}^{+38} \\ 110_{-23}^{+40} \\ 17_{-9}^{+26}$	$\begin{array}{c} 0.97^{+0.18}_{-0.16} \\ 1.04^{+0.15}_{-0.16} \\ 1.06^{+0.16}_{-0.19} \\ 0.75^{+1.02}_{-0.44} \end{array}$	$6.9^{+0.3}_{-0.3}$	$0.166^{+0.017}_{-0.014}$
$\overline{N_T (\text{Total})^{\dagger\dagger}}$			$3.82^{+1.06}_{-0.53} \times 10^{12} \text{ cm}^{-2}$		

Note. The quoted uncertainties represent the 16th and 84th percentile (1σ for a Gaussian distribution) uncertainties, which are derived with the same methods mentioned in Table 3. See Figure B3 for a covariance plot.

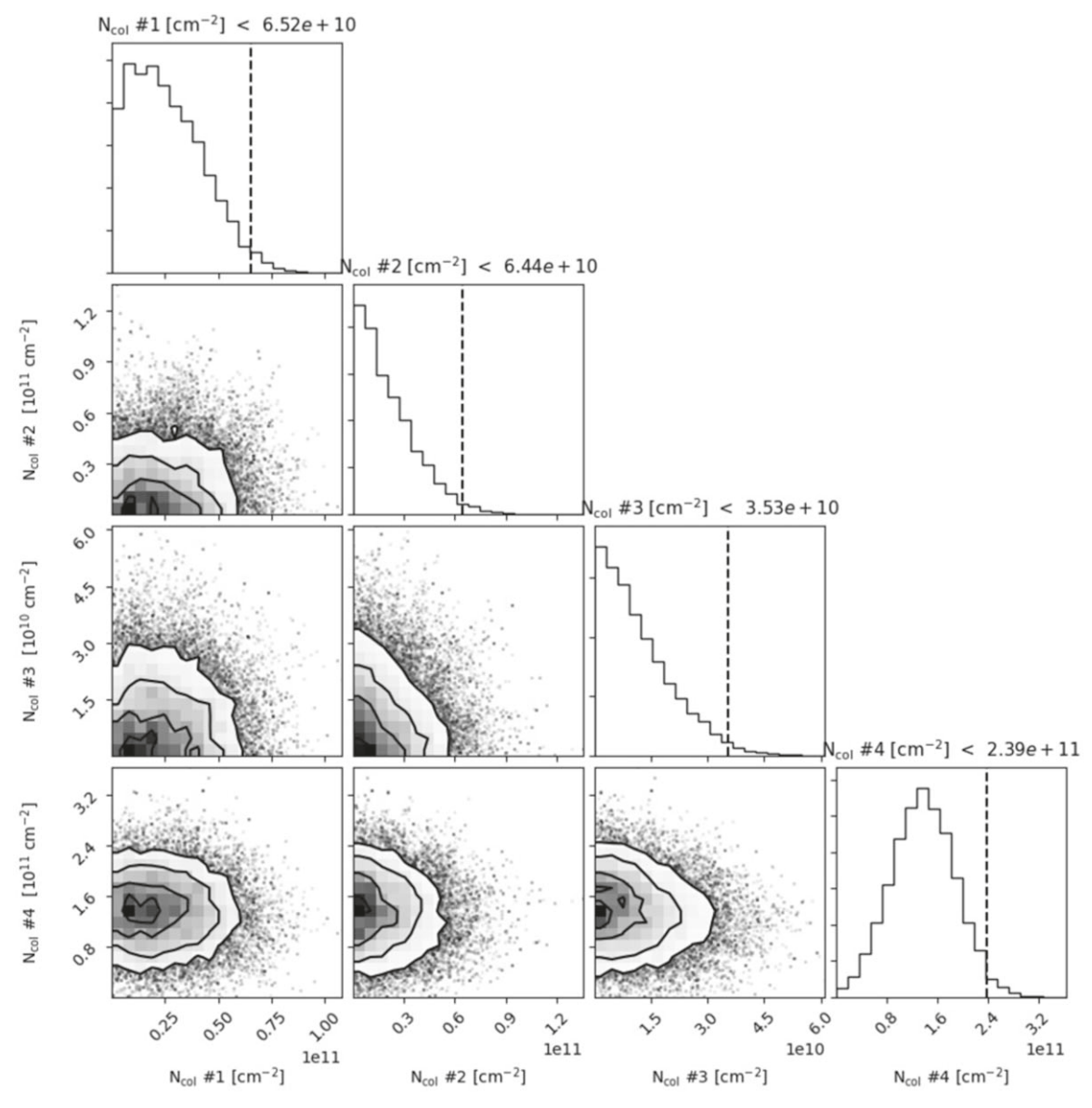


Figure C1. Parameter covariances and marginalized posterior distributions for the HC_6NC MCMC fit. The 97.8th confidence interval (corresponding to 2σ for a Gaussian posterior distribution) is shown as a vertical line.

Appendix C HC₆NC Analysis Results

Following the similar line-selection process with HC₄NC, a total of 10 transitions (including hyperfine components) of

 HC_6NC were considered and the data are again available in GOTHAM Collaboration (2020). In our observation, no signal beyond a 1σ detection limit can be assigned to HC_6NC . Column density upper limits are therefore constrained using the

Component	v_{lsr} (km s ⁻¹)	Size	(10^{11}cm^{-2})	T _{ex} (K)	ΔV (km s ⁻¹)
C1	[5.624]	[33]	< 0.65	[6.5]	[0.117]
C2	[5.790]	[22]	< 0.64		
C3	[5.910]	[50]	< 0.35		
C4	[6.033]	[18]	< 2.39		
$N_T (\text{Total})^{\dagger\dagger}$		<	$< 4.04 \times 10^{11} \text{ cm}^{-1}$	-2	

Note. Upper limits are given as the 97.8th percentile (2σ) value. Parameters in brackets were held fixed to the 50th percentile value. See Figure C1 for a covariance plot.

modified fitting process described in Loomis et al. (2020), the results of which are given in Table C1. A corner plot of the parameter covariances for the HC₆NC MCMC fit is shown in Figure C1.

ORCID iDs

Ci Xue https://orcid.org/0000-0003-2760-2119
Eric R. Willis https://orcid.org/0000-0002-7475-3908
Ryan A. Loomis https://orcid.org/0000-0002-8932-1219
Kin Long Kelvin Lee https://orcid.org/0000-0002-1903-9242
Andrew M. Burkhardt https://orcid.org/0000-0003-0799-0927
Christopher N. Shingledecker https://orcid.org/0000-0002-5171-7568
Martin A. Cordiner https://orcid.org/0000-0001-8233-2436
Michael C. McCarthy https://orcid.org/0000-0002-5450-5894
Eric Herbst https://orcid.org/0000-0002-4649-2536
Anthony J. Remijan https://orcid.org/0000-0001-9479-9287
Brett A. McGuire https://orcid.org/0000-0003-1254-4817

References Acharyya, K., & Herbst, E. 2017, ApJ, 850, 105 Araya, E., Hofner, P., Kurtz, S., Bronfman, L., & DeDeo, S. 2005, ApJS, Balucani, N., Ceccarelli, C., & Taquet, V. 2015, MNRAS, 449, L16 Bell, M. B., Watson, J. K. G., Feldman, P. A., & Travers, M. J. 1998, ApJ, Botschwina, P., Heyl, Ä, Chen, W., et al. 1998, JChPh, 109, 3108 Botschwina, P., Horn, M., Flügge, J., & Seeger, S. 1993, J. Chem. Soc., Faraday Trans., 89, 2219 Broten, N. W., Oka, T., Avery, L. W., MacLeod, J. M., & Kroto, H. W. 1978, ApJL, 223, L105 Brown, R. D. 1977, Natur, 270, 39 Brown, R. D., Burden, F. R., & Cuno, A. 1989, ApJ, 347, 855 Burkhardt, A. M., Herbst, E., Kalenskii, S. V., et al. 2018, MNRAS, 474, 5068 Burkhardt, A. M., Loomis, R. A., Shingledecker, C. N., et al. 2020, NatAs, Calcutt, H., Fiechter, M. R., Willis, E. R., et al. 2018, A&A, 617, A95 Coutens, A., Rawlings, J. M. C., Viti, S., & Williams, D. A. 2017, MNRAS, 467, 737

```
Dobashi, K., Shimoikura, T., Nakamura, F., et al. 2018, ApJ, 864, 82
Gensheimer, P. D. 1997, ApJL, 479, L75
Geppert, W. D., Ehlerding, A., Hellberg, F., et al. 2004, ApJ, 613, 1302
GOTHAM Collaboration 2020, Spectral Stacking Data for Phase 1 Science
  Release of GOTHAM, 4.0, Harvard Dataverse, doi:10.7910/DVN/
Graninger, D., Öberg, K. I., Qi, C., & Kastner, J. 2015, ApJL, 807, L15
Graninger, D. M., Herbst, E., Öberg, K. I., & Vasyunin, A. I. 2014, ApJ,
  787, 74
Gratier, P., Majumdar, L., Ohishi, M., et al. 2016, ApJS, 225, 25
Gratier, P., Pety, J., Guzmán, V., et al. 2013, A&A, 557, A101
Gronowski, M., & Kołos, R. 2006, CPL, 428, 245
Guarnieri, A., Hinze, R., Krüger, M., et al. 1992, JMoSp, 156, 39
Hacar, A., Bosman, A. D., & van Dishoeck, E. F. 2020, A&A, 635, A4
Haykal, I., Margulès, L., Huet, T. R., et al. 2013, ApJ, 777, 120
Herbst, E., Terzieva, R., & Talbi, D. 2000, MNRAS, 311, 869
Hincelin, U., Wakelam, V., Hersant, F., et al. 2011, A&A, 530, A61
Hirota, T., Yamamoto, S., Mikami, H., & Ohishi, M. 1998, ApJ, 503, 717
Hung, T., Liu, S.-Y., Su, Y.-N., et al. 2019, ApJ, 872, 61
Irvine, W. M., & Schloerb, F. P. 1984, ApJ, 282, 516
Kawaguchi, K., Ohishi, M., Ishikawa, S.-I., & Kaifu, N. 1992, ApJL, 386, L51
Kruger, M., Stahl, W., & Dreizler, H. 1993, JMoSp, 158, 298
Larsson, M., Geppert, W. D., & Nyman, G. 2012, RPPh, 75, 066901
Little, L. T., MacDonald, G. H., Riley, P. W., & Matheson, D. N. 1978,
         S. 183, 45P
Loison, J.-C., Wakelam, V., & Hickson, K. M. 2014a, MNRAS, 443, 398
Loison, J.-C., Wakelam, V., Hickson, K. M., Bergeat, A., & Mereau, R. 2014b,
  MNRAS, 437, 930
Loomis, R. A., Burkhardt, A. M., Shingledecker, C. N., et al. 2020, NatAs,
  submitted
López, A., Tercero, B., Kisiel, Z., et al. 2014, A&A, 572, A44
Margulès, L., Tercero, B., Guillemin, J. C., Motiyenko, R. A., & Cernicharo, J.
  2018, A&A, 610, A44
McCarthy, M. C., Lee, K. L. K., Loomis, R. A., et al. 2020, NatAs, submitted
McGuire, B. A. 2018, ApJS, 239, 17
McGuire, B. A., Burkhardt, A. M., Kalenskii, S., et al. 2018, Sci, 359,
McGuire, B. A., Burkhardt, A. M., Loomis, R. A., et al. 2020a, ApJL, 900, L10
McGuire, B. A., Burkhardt, A. M., Shingledecker, C. N., et al. 2017, ApJL,
   843, L28
McGuire, B. A., Loomis, R. A., Burkhardt, A. M., et al. 2020b, Sci, submitted
Miao, Y., & Snyder, L. E. 1997, ApJL, 480, L67
Müller, H. S. P., Schlöder, F., Stutzki, J., & Winnewisser, G. 2005, JMoSt,
Osamura, Y., Fukuzawa, K., Terzieva, R., & Herbst, E. 1999, ApJ, 519, 697
Quénard, D., Vastel, C., Ceccarelli, C., et al. 2017, MNRAS, 470, 3194
Remijan, A. J., Hollis, J. M., Lovas, F. J., Plusquellic, D. F., & Jewell, P. R.
  2005, ApJ, 632, 333
Ruaud, M., Wakelam, V., & Hersant, F. 2016, MNRAS, 459, 3756
Schilke, P., Walmsley, C. M., Pineau Des Forets, G., et al. 1992, A&A,
  256, 595
Stanton, J. F., Gauss, J., Cheng, L., et al. 2017, The Journal of Chemical
  Physics, 21, 214108
Takagi, N., Fukuzawa, K., Osamura, Y., & Schaefer, H. F., I 1999, ApJ,
  525, 791
Takano, S., Masuda, A., Hirahara, Y., et al. 1998, A&A, 329, 1156
Taniguchi, K., Ozeki, H., Saito, M., et al. 2016, ApJ, 817, 147
Tennekes, P. P., Harju, J., Juvela, M., & Tóth, L. V. 2006, A&A, 456, 1037
Turner, B. E., Pirogov, L., & Minh, Y. C. 1997, ApJ, 483, 235
Vastel, C., Kawaguchi, K., Quénard, D., et al. 2018, MNRAS, 474, L76
Vastel, C., Loison, J. C., Wakelam, V., & Lefloch, B. 2019, A&A, 625, A91
Vigren, E., Semaniak, J., Hamberg, M., et al. 2012, P&SS, 60, 102
Wakelam, V., Loison, J. C., Herbst, E., et al. 2015, ApJS, 217, 20
Woon, D. E., & Herbst, E. 2009, ApJS, 185, 273
Xue, C., Remijan, A. J., Burkhardt, A. M., & Herbst, E. 2019, ApJ, 871,
  112
Zeng, S., Quénard, D., Jiménez-Serra, I., et al. 2019, MNRAS, 484, L43
```